Chapter-3

Quenching-Driven Advancements in Functional Properties of High-Temperature Lead-Free Sc, Ga Modified $0.67BiFeO_3$-$0.33BaTiO_3$ Relaxor Ceramics

CHAPTER 3

Quenching-Driven Advancements in Functional Properties of High-Temperature Lead-Free Sc, Ga Modified $0.67BiFeO_3$-$0.33BaTiO_3$ Relaxor Ceramics

3.1 Introduction

As discussed in chapter 1, in the realm of advanced materials, lead-free piezoelectric perovskite ceramics have emerged as a focal point of intensive research due to their exceptional properties, including high piezoelectric coefficients, substantial Curie temperature (T_C), and remarkable dielectric permittivity. These properties render them indispensable for multifaceted applications such as actuators, sensors, piezoelectric energy harvesters, energy storage systems, photovoltaics, and transformers [37], [38], [39], [40], [41], [42]. The urgency to replace toxic lead-based counterparts with environmentally safe alternatives has led to a concentrated exploration of materials like $K_{0.5}Na_{0.5}NbO_3$ (KNN), $BaTiO_3$ (BT), $Bi_{0.5}Na_{0.5}TiO_3$ (BNT) and $BiFeO_3$ (BFO) [43], [51], [52], [53], [54], [55], [56], [57], [179]. These lead-free options, being compliant with environmental directives like the RoHS regulation, have become imperative in global research endeavors [10], [37], [43], [44].

$BiFeO_3$ (BFO), a unique lead-free perovskite multiferroic, possesses a distinctive combination of ferroelectric and magnetic ordering, characterized by a high Curie temperature (T_C) of 825 ℃ and an antiferromagnetic Neel temperature (T_N) of 370 ℃ [16], [65]. This exceptional attribute positions BFO as a highly desirable material for applications demanding resilience under extreme conditions, such as space exploration, nuclear reactors, and oil drilling, where materials must endure temperatures exceeding 300 ℃ [58], [59]. However, despite its potential, challenges persist, including the achievement of pure phase formation, reduction of Fe-valence state, high leakage current, thermodynamic instability, and defect formation [43], [66], [67].

To overcome these challenges, researchers have explored various strategies, including site engineering techniques and the formation of solid solutions with other ABO_3-type perovskites [68], [69], [72], [73], [74]. Notably, the discovery of a morphotropic phase boundary (MPB) in the (1-x)BF-xBT solid solution, spanning a specific composition range of $0.25 < x < 0.4$ between rhombohedral and cubic phases, has accelerated research efforts due to its potential to enhance piezoelectric properties [44], [96], [97]. The proximity to the MPB often results in superior piezoelectric performance [99], [180]. Previous studies have reported significant achievements in this domain, such as the remarkable d_{33} value of ~402 pC/N and T_c of ~454 °C observed by incorporating Ga^{3+} into a $0.67BiFeO_3$-$0.33BaTiO_3$ which typically creates MPB and improves both insulation and electromechanical properties [31], [100]. The integration of relaxor properties into ferroelectric materials has been a topic of intense exploration, with methods like isovalent substitution and grain size reduction demonstrating significant potential [181]. Chemical modifications with rare earth elements, particularly Sc, have been particularly successful, effectively suppressing impurity phases and enhancing magnetic properties, while also reducing leakage current density [182], [183], [184].

In the context of bulk $BiFeO_3$-$BaTiO_3$ (BF-BT) ceramics, the influence of processing methods and site engineering techniques on functional properties has been widely acknowledged [105], [106]. Noteworthy studies by Kim et al. emphasized the impact of specific cooling rates, revealing enhanced properties in air-quenched samples of specific compositions [108]. Additionally, investigations by Ji et al. comparing microwave and conventional sintering methods highlighted reduced grain size, lower dielectric loss, and decreased ferroelectric properties in microwave-sintered samples [109]. Furthermore, Lee et al. demonstrated improved piezoelectric responses in BF-BT

compositions through tailored cooling and heating processes, underscoring the critical role of precise thermal treatments [110].

However, despite these advancements, a comprehensive comparative study between air quenching sintering and conventional closed sintering for the specific MPB composition of 0.67BF-0.33BT is notably absent in the existing literature. We have strategically incorporated isovalent Sc and Ga substitutions at the Fe-site in a MPB composition of 0.67BF-0.33BT, along with 5 mol % excess Bi_2O_3, to overcome existing limitations. Investigation presented in this chapter, meticulously compares two distinct processing methods: closed sintering and air quenching exploring their effects on the material's structure and properties, encompassing phase structure, microstructure, and electrical characteristics.

In our systematic analysis, we observed that the air-quenched samples exhibited exceptional features, including T_{max} values surpassing 400 °C, low dissipation factor, and high dielectric constant across various temperatures and frequencies. These findings highlight the suitability of air-quenched ceramics for high-temperature applications. Our study provides crucial insights into the interplay between composition, processing methods, and functional properties of lead-free perovskite ceramics, opening avenues for innovative materials design and applications in challenging environments.

3.2 Experimental Procedure

3.2.1 Sample preparation

The lead-free ceramic specimens of composition, $0.67\{Bi(Fe_{0.97}Ga_{0.03})_{1-x}Sc_xO_3\}$-$0.33(BaTiO_3)$, with x=0.01 (Sc1), 0.02 (Sc2), 0.03 (Sc3), 0.04 (Sc4), 0.05 (Sc5), 0.06 (Sc6) and 0.07 (Sc7) were prepared for the present investigation. To prepare these compositions, a modified traditional solid-state reaction method was employed, utilizing

two different sintering techniques: air quenching (AQ) and closed sintering (CS). The methodology for sample preparation is depicted in Figure 3.1. The high purity (>99%) analytical reagent grade metal oxides powders of Bi_2O_3 (99.9% Sigma Aldrich), Fe_2O_3 (99% Hi Media), Ga_2O_3 (99.9%, Alfa Aesar), Sc_2O_3 (99.9%, Sigma Aldrich), $BaCO_3$ (99%, Sigma Aldrich) and TiO_2 (99%, Sigma Aldrich) were weighed according to the nominal stoichiometric ratio and then suspended in ethanol media. A planetary ball mill (Retsch-PM 400 GmbH and Rheinische, Germany) was used to mix the powders at 300 rpm for 24 hours, using 5 mm, stabilized zirconia balls. It should be noted that. an excess of 5 mol% Bi_2O_3 was added to compensate for the volatilization of Bi_2O_3 during high-temperature heat treatments.

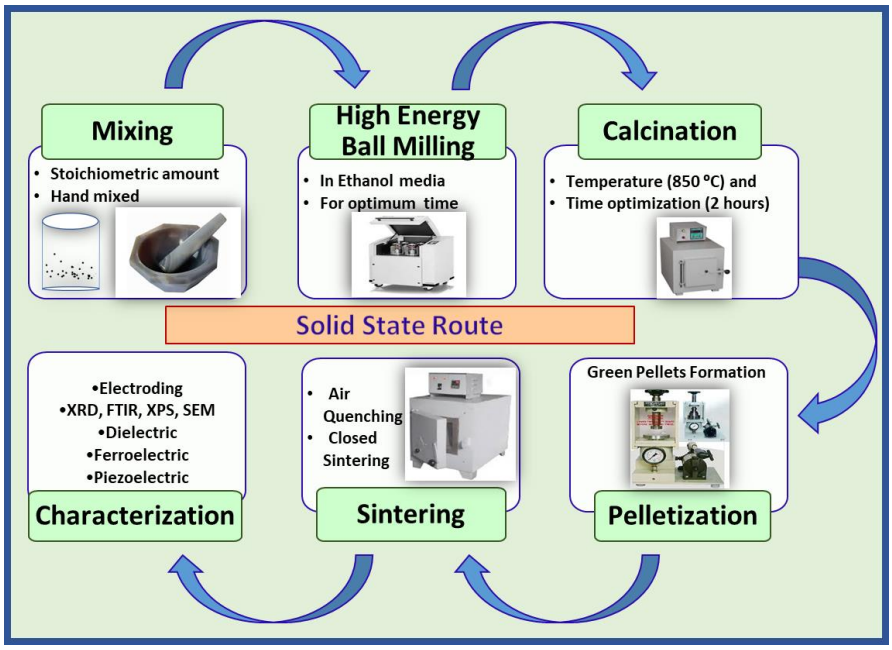

Figure 3.1 The schematic diagram for methodology adopted to prepare $0.67\{Bi(Fe_{0.97}Ga_{0.03})_{1-x}Sc_xO_3\}$-$0.33(BaTiO_3)$ ceramics, where x=0.01 to 0.07.

The obtained wet slurry was subjected to drying at 120 °C, resulting into milled powder. Subsequently, the powder was calcined at 850 °C for 2 hours. After calcination, it was thoroughly mixed with a 2 wt.% polyvinyl alcohol (PVA) water solution, which acted as a binding agent. Uniaxial pressing using a hydraulic press (Osho Scientific, India)

was employed to form 10 mm pellets in a cylindrical steel die, with optimized load of 100 kN. To remove the binder, the pellets were heated at 550 ℃ for 12-hours.

For sintering, two distinct methods were employed: closed sintering (CS) and air quenching (AQ) at 960 ℃ for two hours. In the CS method, the pellet was sintered inside an inverted alumina crucible sealed with MgO powder. A certain amount of spacer powder of the same composition was also kept inside the crucible to prevent Bi-loss during sintering. To ensure precise control over the air quenching sintering process, the prepared pellet was kept in an open-air environment within a muffle furnace. To prevent the loss of Bismuth at higher temperatures, rapid heating was carried out at a rate of 9 ℃/min. Once the sample had completed the designated dwelling time period of 2 hours inside the furnace, it was promptly quenched to room temperature. This quenching process involved swiftly removing the sample from the furnace and placing it at room temperature in open air. For sintering, the heating rate for CS and AQ was maintained at 5 ℃/min and 9 ℃/min, respectively.

The bulk density (ρ_{bulk}) of the sintered pellets was determined using the Archimedes method and ranged from 7.05 g/cm^3 to 7.47 g/cm^3 (corresponding to 94.6% to 99% of the theoretical density). The theoretical density (ρ_t) was calculated using lattice parameters obtained from X-ray diffraction (XRD) data through Rietveld refinement. The relative density (ρ_{rel}) of samples was calculated using the relation $\rho(rel) = \rho(bulk) / \rho(t)$. This information provides insights into the sintering process and the density characteristics of the prepared samples. By employing these two sintering methodologies, the ceramic specimens were successfully synthesized, allowing for further investigation of their properties and performance.

3.2.2 Characterizations

The crystal structures of crushed sintered pellets which were annealed at 550 ℃ for 16 hours were elucidated via high resolution XRD (Rigaku Smartlab 9 kW, Japan) using Cu Kα radiation with a 2θ step size of 0.01º for Rietveld structure refinement while 5 kW rotating anode (Cu) Rigaku diffractometer with a 2θ step size of 0.02º was used for confirmation of phase formation. The phase formation was further confirmed by Fourier transform infrared spectroscopy (FTIR) (Nicolet Summit, Thermo Fisher Scientific, USA) at room temperature in KBr mode with 16 scans and a resolution of 4 cm^{-1}. The structural analysis from the XRD pattern was done using Le-Bail profile matching and Rietveld structure refinement using "FullProf Suite" software. The microstructures of gold sputtered sintered pellets were examined using scanning electron microscope (SEM, ZEISS). The flat surfaces of the pellets were polished and then coated with silver paint for electrical measurements. The silver electrodes were cured at 550 ℃ for 30 minutes. Temperature-dependent dielectric permittivity $\varepsilon_r(T)$ and dielectric loss, tan $\delta(T)$ in the frequency range 20 Hz to 10 MHz (Keysight E4990A, Agilent software) were measured using an impedance analyzer with computerized furnace system maintaining heating and cooling rates of 2 ℃ per minute from 30 ℃ to 500 ℃. The ferroelectric hysteresis (P-E) loops, current response, leakage current, and resistivity were measured at 10 Hz ac-signal using Precision Premier LC II, ferroelectric loop tracer, from Radiant Technologies, USA. For piezoelectric measurements, the samples were poled at 60 ℃-90 ℃ for 30 min in a silicone oil bath by applying 40 kV/cm DC electric field. The low field piezoelectric charge coefficient (d_{33}) was measured using Berlincourt quasistatic d_{33} meter PIEZOTEST (UK) at 0.25 N force and 110 Hz frequency. To examine the chemical states of the Fe and O elements, X-ray photoelectron spectroscopy (XPS) was employed using the Thermo Scientific K-Alpha instrument. These characterization techniques provided

valuable insights into the structural, electrical, and chemical properties of the studied lead-free ceramic specimens.

3.3 Results and discussion

3.3.1 Structural analysis

3.3.1.1 Crystal Structure Analysis

The XRD patterns of the prepared compositions using AQ and CS methods at 960 ^{0}C for two hours are depicted in Figure 3.2. The XRD patterns show that the $0.67\{Bi(Fe_{0.97}Ga_{0.03})_{1-x}Sc_xO_3\}$-$0.33(BaTiO_3)$ samples exhibit the perovskite crystal structure, with no detectable reactant impurities for all the compositions prepared. This indicates that the Sc^{3+} and Ga^{3+} cations are fully incorporated into the BF-BT lattice. A negligibly small secondary phase XRD peak corresponding to $Bi_2Fe_4O_9$ or $Bi_{25}Fe_4O_{39}$ was found in lower doping concentration compositions [185], [186].

As the doping concentration of Sc increases the formation of the pure perovskite phase is promoted in BF-BT, which results in improved electrical properties [97], [187]. The absence of apparent peak splitting suggests that the primary phase in these samples has cubic symmetry at room temperature.

The Rietveld structure refinement fit for the XRD patterns of Sc CS and Sc AQ compositions are presented in Figure 3.3 (a-j). A prominent (111) peak is observed around 39°, indicating the presence of the pseudocubic phase with the space group $Pm\bar{3}m$. The absence of peak splitting confirms the cubic symmetry of the phase. On increasing the doping concentration of Sc, the lattice parameter remains unchanged, and no crystallographic phase transition takes place. The goodness of fit parameter (χ^2) is found to be 1.19 to 2.26 respectively, indicating a quite good fit between the experimental and calculated XRD data. For instance, in the case of the Sc2 and Sc7 compositions with AQ method, the Rietveld crystal structure refinement reveals that the structure is a mixture of

the major cubic ($Pm\bar{3}m$) and minor rhombohedral ($R3c$) phases as shown in Fig 3.3 (b and d). The lattice parameter for the cubic phase of Sc2 AQ and Sc7 AQ are 3.9967(5) Å and 3.9997(6) Å, respectively. The lattice parameters derived from Rietveld refinement for the rhombohedral structure of Sc2 AQ and Sc7 AQ are a_H=5.6121(9) Å, c_H=13.9207(4) Å, and a_H=5.6260(1) Å, c_H=13.7806(1) Å, respectively, considering a hexagonal unit cell choice. The unit cell volumes are calculated as V_C=63.842(1) Å^3 and V_C=63.989(2) Å^3 for the Sc2 AQ and Sc7 AQ samples, respectively.

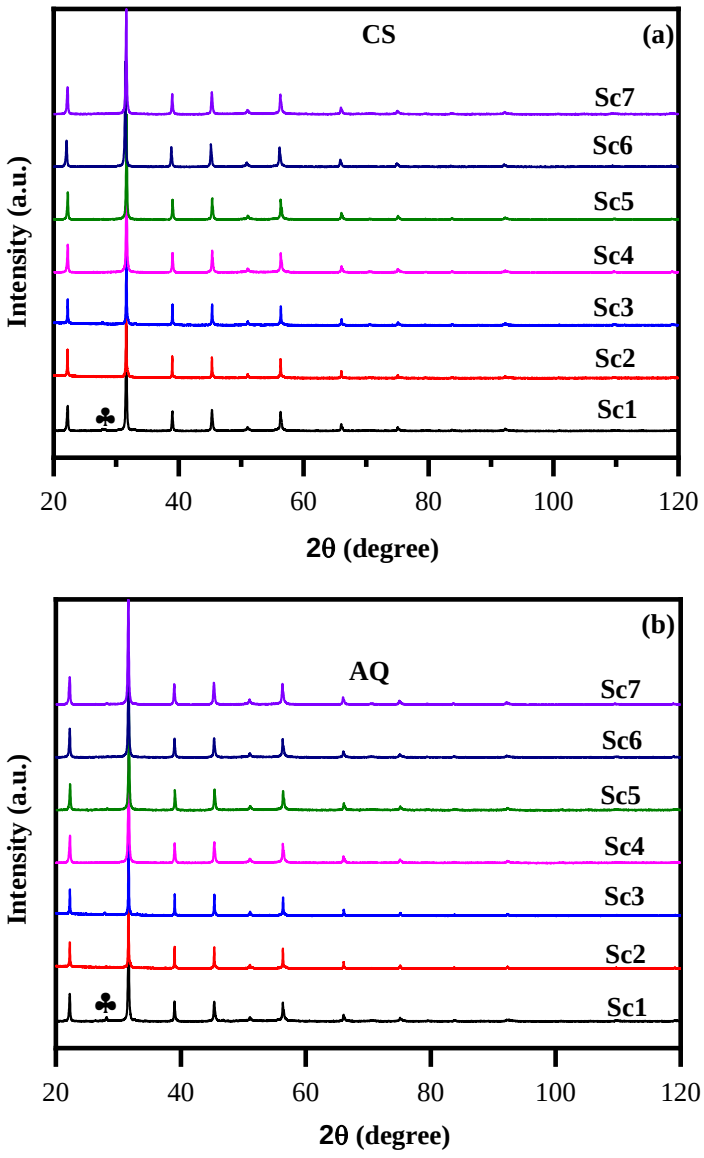

Figure 3.2 XRD patterns of 0.67{$Bi(Fe_{0.97}Ga_{0.03})_{1-x}Sc_xO_3$}-0.33($BaTiO_3$) samples prepared using (a) CS and (b) AQ methods.

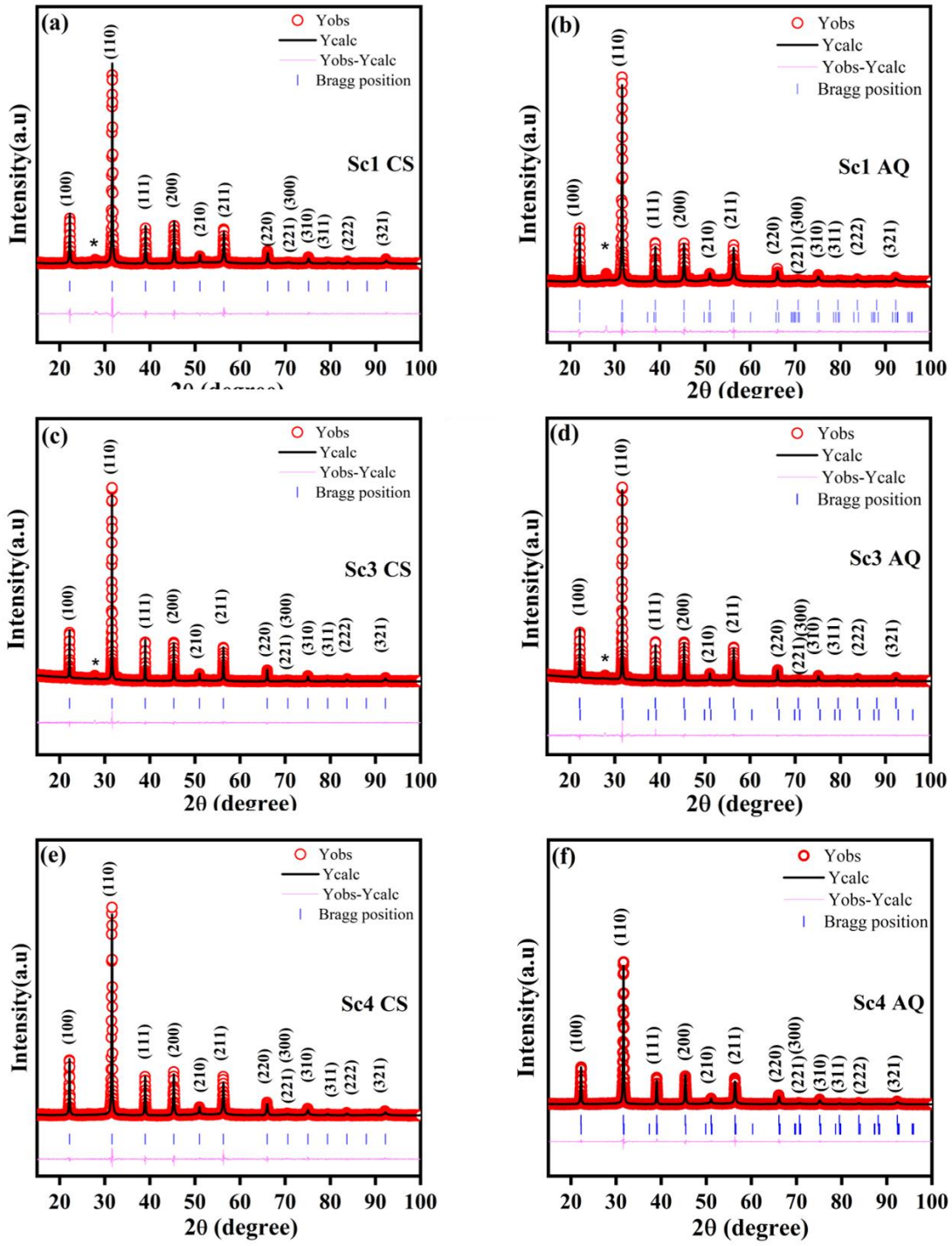
(a)
Yobs
Ycalc
Yobs-Ycalc
Bragg position
Sc1 CS
Intensity(a.u)
(100)
(110)
(111)
(200)
(210)
(211)
(220)
(221) (300)
(310)
(311)
(222)
(321)
*
20 30 40 50 60 70 80 90 100
(b)
Sc1 AQ
2θ (degree)
(c)
Sc3 CS
(d)
Sc3 AQ
(e)
Sc4 CS
(f)
Sc4 AQ

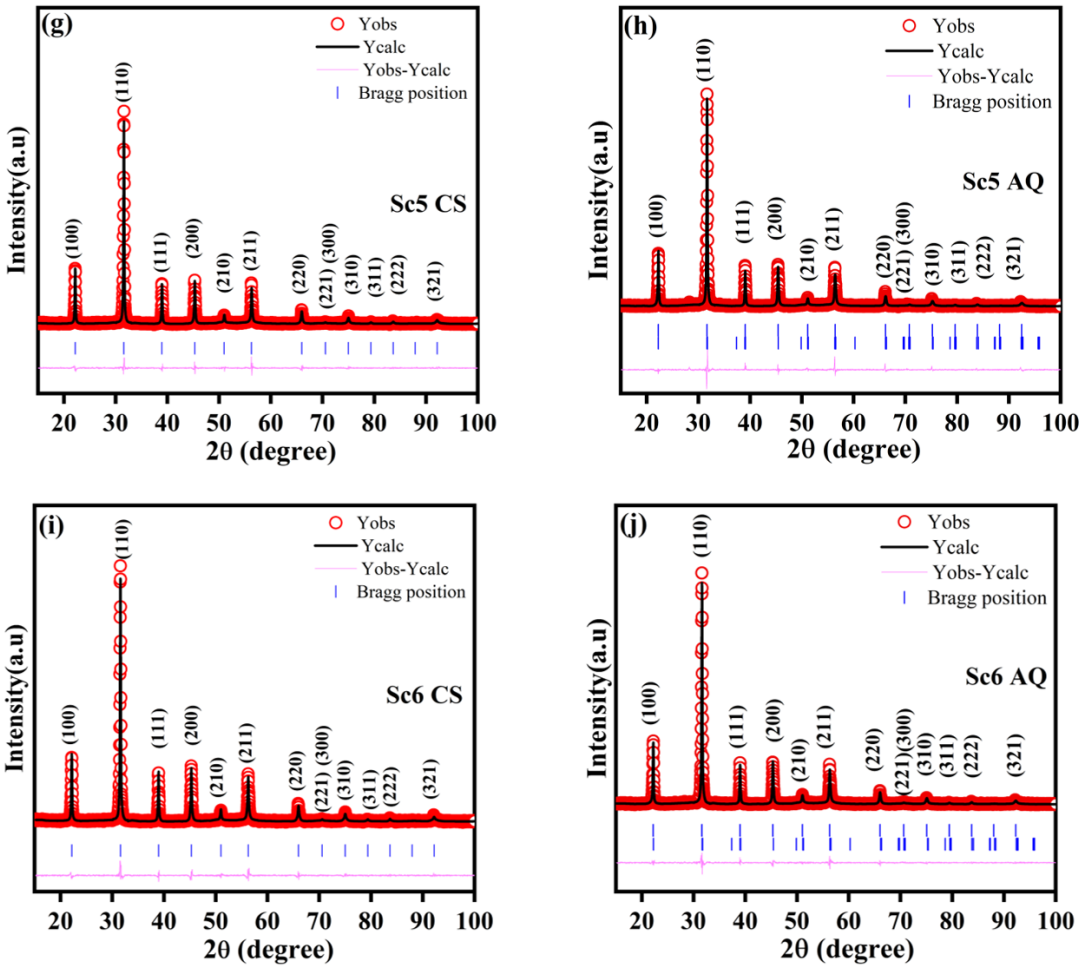

Figure 3.3 Rietveld refinement fits for (a) Sc1 CS, (b) Sc1 AQ, (c) Sc3 CS, (d) Sc3 AQ, (e) Sc4 CS, (f) Sc4 AQ, (g) Sc5 CS, (h) Sc5 AQ, (i) Sc6 CS and (j) Sc6 AQ samples.

The goodness of fit parameters (χ^2) are 1.51 and 1.41, respectively. Table 3.1 lists the detailed information about lattice parameters (a and c), unit cell volume (V), and goodness of fit parameter (χ^2) obtained from the Rietveld analysis for all prepared samples. The addition of the second phase (R3*c*) in the AQ samples improves the χ^2 factors, suggesting a more accurate representation of the crystal structure. This observation aligns with previous literature where the pseudocubic phase is reported for undoped samples and the R3*c* phase is reported to be induced in air quenched ceramics [100], [188]. Overall, the XRD analysis confirms the presence of the pseudocubic phase

in the CS sample and the coexistence of cubic and rhombohedral phases in the AQ sample.

Table 3.1 Lattice parameters, space group, and refinement factors for all CS and AQ samples compositions.

Composition	Space Group [Phase fraction]	Lattice parameter Å	R_p	R_{wp}	R_{exp}	χ^2
Sc1 CS	P$m\bar{3}m$ [100.0%]	a=b=c=3.9948(1)	10.8	13.3	8.86	2.26
Sc1 AQ	P$m\bar{3}m$ [86.6(3) %] + R3c [13.3(7) %]	a_c=3.9959(4) a_H=5.6310(6) c_H=13.9485(4)	10.6	14.2	11.1	1.62
Sc2 CS	P$m\bar{3}m$ [100.0%]	a=b=c=3.9964(1)	6.83	8.97	6.44	1.94
Sc2 AQ	P$m\bar{3}m$ [82.0(9) %] + R3c [17.9(1)%]	a_c=3.9967(5) a_H=5.6121(9) c_H=13.9207(4)	6.15	7.80	6.36	1.51
Sc3 CS	P$m\bar{3}m$ [100.0%]	a=b=c=3.9990(3)	5.64	7.10	6.51	1.19
Sc3 AQ	P$m\bar{3}m$ [89.2(7)%] + R3c [10.7) %]	a_c= 3.9948(7) a_H=5.6260(9) c_H=13.7807(6)	5.71	7.39	6.62	1.24
Sc4 CS	P$m\bar{3}m$ [100.0%]	a=b=c=3.9991(3)	10.9	14.0	11.7	1.44
Sc4 AQ	P$m\bar{3}m$ [92.6(3) %] + R3c [7.3(7) %]	a_c= 3.9945(3) a_H= 5.6315(7) c_H=13.8395(1)	8.29	10.8	9.08	1.41
Sc5 CS	P$m\bar{3}m$ [100.0%]	a=b=c=4.0009(4)	10.1	13.4	11.3	1.39
Sc5 AQ	P$m\bar{3}m$ [87.3(6) %] + R3c [12.6(4)%]	a_c=3.9902(1) a_H= 5.6315(7) c_H=13.8395(1)	11.4	14.7	11.5	1.63
Sc6 CS	P$m\bar{3}m$ [100.0%]	a=b=c=4.0000(5)	9.94	12.9	9.93	1.68
Sc6 AQ	P$m\bar{3}m$ [88.6(1) %] + R3c [11.3(9) %]	a_c= 3.9968(4) a_H= 5.6315(7) c_H=13.8395(1)	9.91	13.0	11.3	1.34

Sc7 CS	P$m\bar{3}m$ [100.0%]	a=b=c=3.9964 (1)	9.01	11.6	8.81	1.74
Sc7 AQ	P$m\bar{3}m$ [90.2(3)%] + R3c [9.7(7) %]	a_c=3.9997(6) a_H=5.6260(1) c_H=13.7806(1)	8.67	9.67	8.81	1.41

3.3.1.2 FTIR Studies

Figure 3.4 presents the FTIR spectra of all prepared AQ and CS samples, spanning the wavenumber range of 400-4000 cm^{-1}. In this range, all samples exhibit a broad absorption band between 3300-3600 cm^{-1}, indicating symmetric and antisymmetric stretching of hydroxyl ions and H_2O molecules, respectively. Additionally, a band at 1632 cm^{-1} corresponds to the bending vibration of H_2O [189]. An absorption band at approximately 2924 cm^{-1} arises from OH^- stretching due to the hygroscopic nature of KBr powder used in pellet preparation with sintered sample powder, as there is no characteristic peak in the region 1000-4000 cm^{-1} [190]. The distinctive and strong absorptive peaks observed solely in the region between 400-600 cm^{-1} can be attributed to the stretching and bending vibration modes of Ti-O, Fe-O, and Bi-O, corresponding to the 'signature TiO_6/FeO_6 octahedral groups'. These peaks, in conjunction with the bands for metal-oxygen, serve as confirmation of the formation of the perovskite phase [190], [191], [192], [193]. The average bond lengths (r) of Fe-O and/or Ti-O bonds were calculated using the wavenumbers corresponding to sharp peaks in the 400-600 cm^{-1} region obtained for each composition from FTIR spectra, as detailed in Table 3.2.

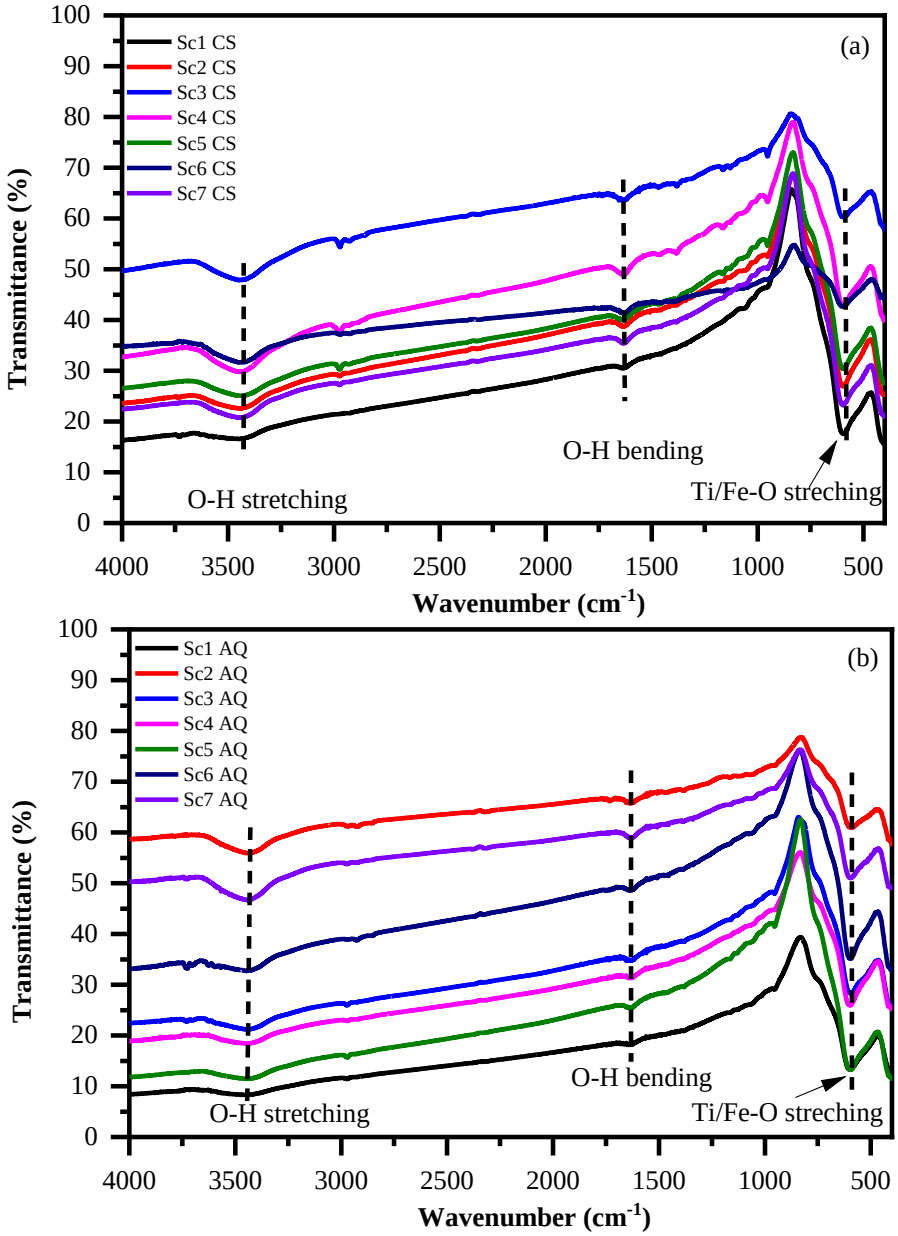

Figure 3.4 presents the FTIR spectra of all prepared (a) CS and (b) AQ samples, spanning the wavenumber range of 400-4000 cm^{-1}.

The vibrational frequency of a bond can be calculated by the relation $\nu = \frac{1}{2\pi c}\left(\frac{k}{\mu}\right)^{\frac{1}{2}}$; where 'ν' defines the wavenumber of the absorption band corresponding to a particular bond, 'k' is the force constant of the bond, 'c' is the velocity of light. The parameter 'μ' is the reduced or effective mass of a bond given by the relation $\mu = \frac{m_O * m_X}{m_O + m_X}$;

where 'm_o' is the atomic weight of oxygen and 'm_x' can be the atomic weight of Fe, Ti, or Bi. Further for the calculation of the bond length, we can use the relation $k = \frac{17}{r^3}$. The calculated values of different parameters obtained from these relations are given in the tabular form in Table 3.2.

Table 3.2 Wavenumber, effective mass, frequency of vibration, force constant, and bond length of Fe-O bond for investigated Sc, Ga substituted BF-BT samples prepared by closed sintering (CS) and air quenching (AQ) methods.

Composition	Wavenumber υ (cm^{-1})	Effective Mass (μ) (10^{-26})	Frequency of vibration (f) (Hz) (10^{13})	Force Constant k (N/cm)	Bond length Ti/Fe-O r(Å)
CS					
Sc1	594.671	2.0644	1.7840	2.5912	1.8720
Sc2	595.180	2.0644	1.7855	2.5957	1.8709
Sc3	593.389	2.0644	1.7802	2.5801	1.8747
Sc4	594.141	2.0644	1.7824	2.5866	1.8731
Sc5	593.874	2.0644	1.7816	2.5843	1.8737
Sc6	603.370	2.0644	1.8101	2.6677	1.8539
Sc7	595.433	2.0644	1.7863	2.5979	1.8704
AQ					
Sc1	599.019	2.0644	1.7971	2.6292	1.8629
Sc2	592.977	2.0644	1.7789	2.5765	1.8755
Sc3	593.642	2.0644	1.7809	2.5822	1.8742
Sc4	599.69	2.0644	1.7991	2.6352	1.8616
Sc5	598.329	2.0644	1.7949	2.6232	1.8644
Sc6	594.811	2.0644	1.7844	2.5925	1.8717
Sc7	592.991	2.0644	1.7789	2.5766	1.8756

The representative ball stick model of perovskite unit cell plotted in VESTA using cif file generated from Rietveld refinement is shown in Figure 3.5. The Ti/Fe-O bond lengths (in Å) were calculated using VESTA software using Rietveld refinement results. For the CS compositions, the bond lengths were found to be 1.9974(1) Å, 1.9982(4) Å, 1.9995(2) Å, 1.9995(7) Å, 2.0004(7) Å, 2.0000(3) Å, and 2.0019(1) Å, organized in increasing order of doping concentration from Sc1 to Sc7. In the case of AQ compositions, the Ti/Fe-O bond lengths were 1.9979(7) Å, 1.9983(3) Å, 1.9974(3) Å, 1.9972(7) Å, 1.9951(1) Å, 1.9984(1) Å, and 1.9998(8) Å, similarly arranged based on ascending doping

concentration. The bond length calculations confirm the Ti/Fe-O bond formation, which assures the development of (Ti/Fe)O_6 octahedron in the prepared samples and are in close agreement with the (Ti/Fe)-O bond length calculated from Rietveld refinement. The variation in the bond length with composition is non-linear which might be attributed to different octahedral distortion. Charge separation and permanent polarization are anticipated to result from such distortion, helping to improve the materials dielectric characteristics.

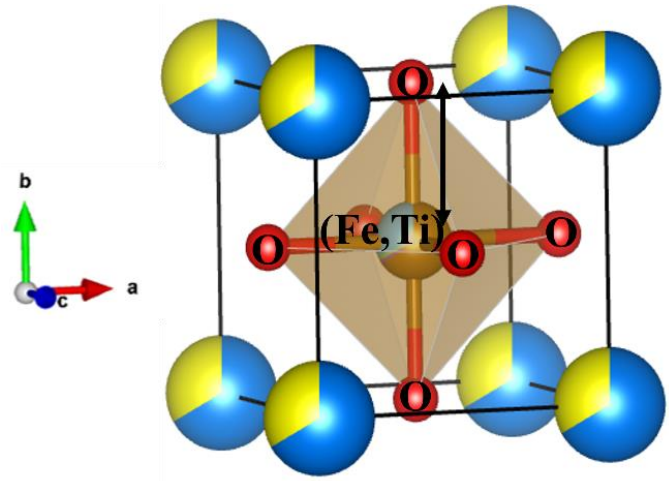

Figure 3.5 Ball and Stick model plotted using VESTA with obtained CIF file of Sc2 CS Rietveld refinement results representing the Ti/FeO_6 octahedron and Ti/Fe-O bonds.

3.3.1.3 XPS Studies

The electronic states of AQ and CS samples were investigated using XPS characterization, exploring the impact of chemical composition, valence states of ions, and processing methods. As illustrated in Figure 3.6 (a), the XPS analysis confirmed the presence of specific peaks corresponding to different ions, namely O 1s, Fe $2p_{1/2}$, Fe $2p_{3/2}$, Bi $4f_{7/2}$, Bi $4f_{5/2}$, Ba $3d_{5/2}$, Ba $3d_{3/2}$, Ti $2p_{3/2}$, Ti $2p_{1/2}$, Ga $3d_{5/2}$, Ga $3d_{3/2}$, Sc $2p_{3/2}$, and C 1s, in the obtained XPS survey spectrum. Notably, no undesired elements were detected. Peak fitting was performed using Gaussian and Lorentzian distribution functions, along with Shirley background, in CASA XPS software to analyze the XPS data. The binding

energy of the C 1s signal at 284.8 eV served as the reference for calibrating the binding energies of other photoelectron peaks in the analysis. In the context of defect chemistry, the evaporation of bismuth in BFO-based piezoceramics can alter stoichiometry, leading to the induction of Bi vacancies (V_{Bi}''') and oxygen vacancies ($V_O^{\bullet\bullet}$) or other defects to maintain the charge neutrality as a result of reduction of Fe^{+3} to Fe^{+2}. The possible defect reaction for the formation of oxygen vacancies due to bismuth evaporation, using the Kröger-Vink notation, can be represented as follows:

$$2Bi_{Bi}^{x} + 3\,O_O'' \rightarrow 2\,V_{Bi}''' + 3V_O^{\bullet\bullet} \qquad (3.1)$$

The presence of the V_{Bi}''' - $V_O^{\bullet\bullet}$ defect dipole is unlikely, as we have confirmed the +3-oxidation state of Bi through the XPS fitting of two Bi 4f components, namely Bi $4f_{7/2}$ at approximately 157.99 eV and Bi $4f_{5/2}$ at 163.29 eV, separated by ~5.3 eV, as shown in Fig 3.6 (b). Due to the highly stable nature and isovalent substitution of Sc^{3+} (0.745 Å) at Fe^{3+} (0.645 Å) sites, it contributes to the stability of the B-site and is not expected to significantly impact defect chemistry. To investigate the influence of sintering and substitution on the oxygen state, the XPS spectra of O 1s signals in the range of 535-525 eV were examined, as shown in Figure 3.6 (c-h). The deconvolution of the asymmetric O 1s peak resulted in three component peaks. The peak around a lower binding energy of 529 eV is generally attributed to lattice O^{2-} ions in the BF-BT structure, while the peak in the vicinity of a higher binding energy of 531 eV (O_V) and 532 eV (O_{ads}) was associated with O^-/O^{2-} ions induced by oxygen vacancies and adsorbed OH respectively [194], [195]. With the increase in the doping concentration of Sc^{3+}, a non-uniform but slight reduction in the number of oxygen vacancies is observed. The ratio of area under the fitted peaks revealed that CS samples exhibited a higher concentration of oxygen vacancies as compared to the AQ samples.

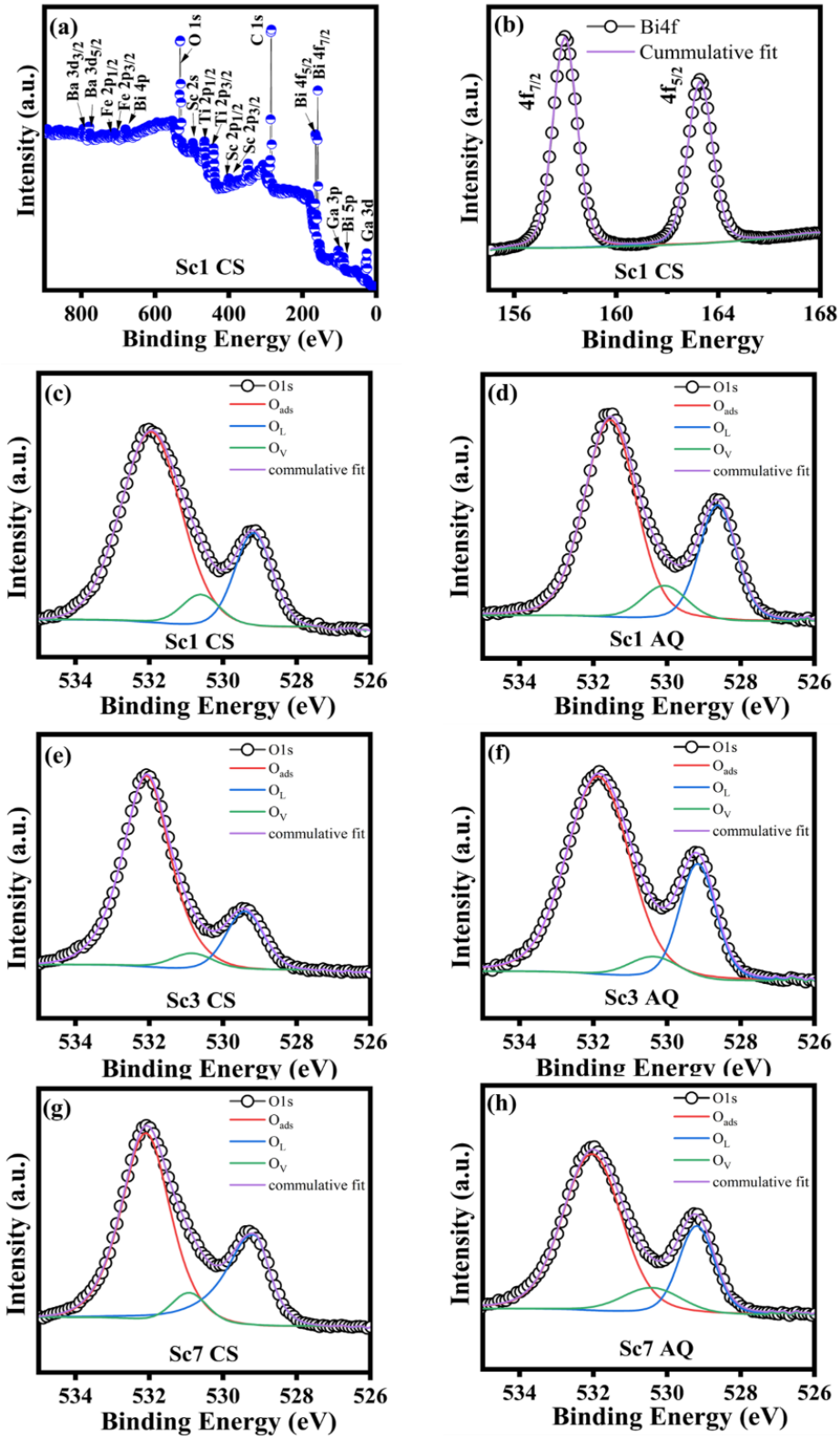

Figure 3.6 XPS spectra of (a) complete spectrum, (b) Bi 4f spectra of Sc1 CS, (c-h) O 1s for Sc1, Sc3 and Sc7 composition samples prepared using AQ and CS method.

In closed sintering, the presence of defect oxygen vacancies ($V_O^{\bullet\bullet}$), can become significantly prominent due to the slow cooling process following sintering, as compared to rapid cooling in air quenching. During the cooling phase within the temperature range of 447 ℃ to 767 ℃, the creation of defects and the development of secondary phases take place [102].

The defect reaction for the formation of oxygen vacancies due to reduction of Fe^{3+} can be given as [196];

$$2Fe_{Fe}^{x} + O_O'' \rightarrow Fe_{Fe}' + V_O^{\bullet\bullet} + O_2 (\uparrow) \qquad (3.2)$$

The valence state of Fe ion was identified using XPS, as depicted in Fig. 3.7. The deconvolution of the Gaussian-Lorentzian fitted Fe $2p_{3/2}$ peak resulted in two components at approximately 709 eV and 710 eV, respectively. These results indicate the presence of distinctive valence states of iron in +2 (~709 eV) and +3 (~710 eV) states in all the prepared samples due to the reduction of Fe^{3+} to Fe^{2+} as a result of capturing the electron resulting from oxygen vacancy creation [197]. The peak area ratio evaluation of Fe^{2+}/Fe^{3+} for Sc1 CS, Sc3 CS, Sc5 CS, and Sc7 CS is 30/70, 30/70, 32/68 and 32/68, respectively meanwhile the same ratio for Sc1 AQ, Sc3 AQ, Sc5 AQ, and Sc7 AQ is 39/61, 30/70, 37/63 and 36/64 respectively showing a little difference in ratios due to the different sintering conditions. The evaluation of the peak area ratio of Fe^{2+}/Fe^{3+} further demonstrates the prevalence of the Fe^{3+} state in all specimens. Through the analysis of the Fe 2p and O 1s states in the peak area, we observed a similar irregular pattern in both Fe^{2+} and $V_O^{\bullet\bullet}$ confirming the anticipated link between oxygen vacancy formation and iron reduction. Typically, when the number of oxygen vacancies decreases, it leads to a decrement in the reduction of valence of iron (Fe) from Fe^{+3} to Fe^{+2}.

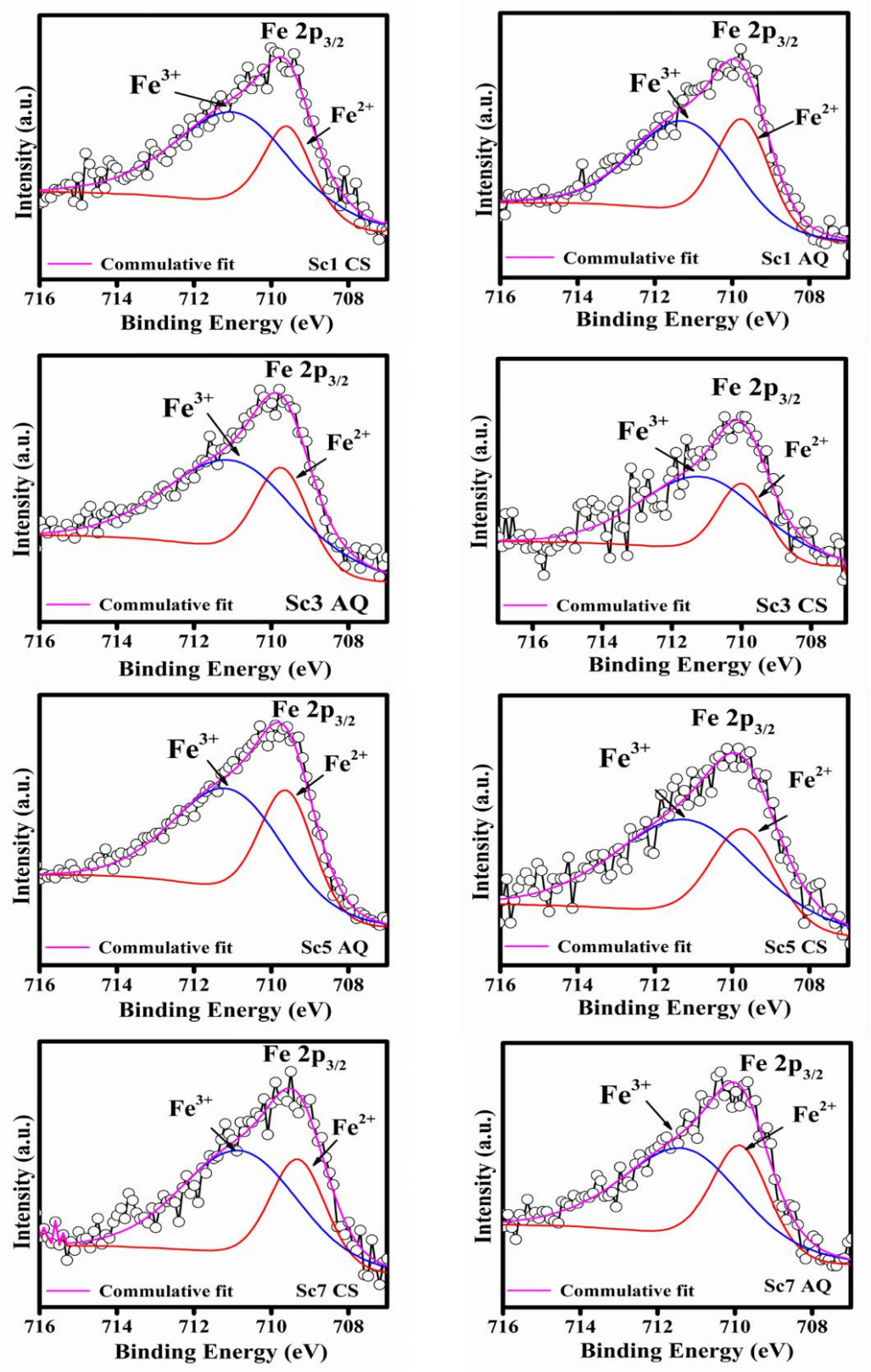

Figure 3.7 XPS spectra of Fe $2p_{3/2}$ for Sc1, Sc3, Sc5, and Sc7 samples, prepared using AQ and CS methods.

Furthermore, this reduction is accompanied by a decrease in the formation Fe'_{Fe} - $V_O^{\bullet\bullet}$ defect dipoles which leads to better functional properties as the defect dipoles, Fe'_{Fe} - $V_O^{\bullet\bullet}$ and V_{Bi}''' - $V_O^{\bullet\bullet}$ create hindrance in domain switching [73].

3.3.2 Microstructure Analysis

Figure 3.8 illustrates the comparison of SEM micrographs of as-sintered ceramic compositions of Sc and Ga substituted BF-BT for both AQ and CS samples, scaled at 1 μm, along with the corresponding grain size distribution. All the prepared samples were effectively sintered at 960 ℃ for 2 hours, yielding bulk densities ranging from 7.05 g/cm^3 to 7.47 g/cm^3 (relative densities of 94.6% to 99%), as determined by the Archimedes method. The micrographs demonstrate homogeneous and uniformly dense microstructures with minimal porosity across all compositions. The grain size distribution is narrow, with an overall average grain size of less than 2 μm. Grain size distributions were evaluated using more than 100 grains, and the statistical distribution is depicted in the insets of each SEM micrograph, exhibiting a consistent Gaussian distribution. The precise enhanced bimodal grain size distribution with comparatively large grains simultaneously distributed among small grains can be observed in all AQ samples in contrast to CS, partly due to quenching effects [198]. The smaller polar nano-grains embedded at the boundary of large grains create hindrance in the formation of long-range ordering which subsequently might be responsible for diffuse phase transitions. The average grain size of the air quenched samples is slightly greater than that of closed sintered samples of the same composition with clearly visible grain boundaries. Ambiguous grain boundaries and diffused grain growth are observed in some CS samples

in contrast to distinct grain boundaries in AQ samples; this may be due to slow cooling and lower heating rate of CS samples or may be due to a closed atmosphere sintering.

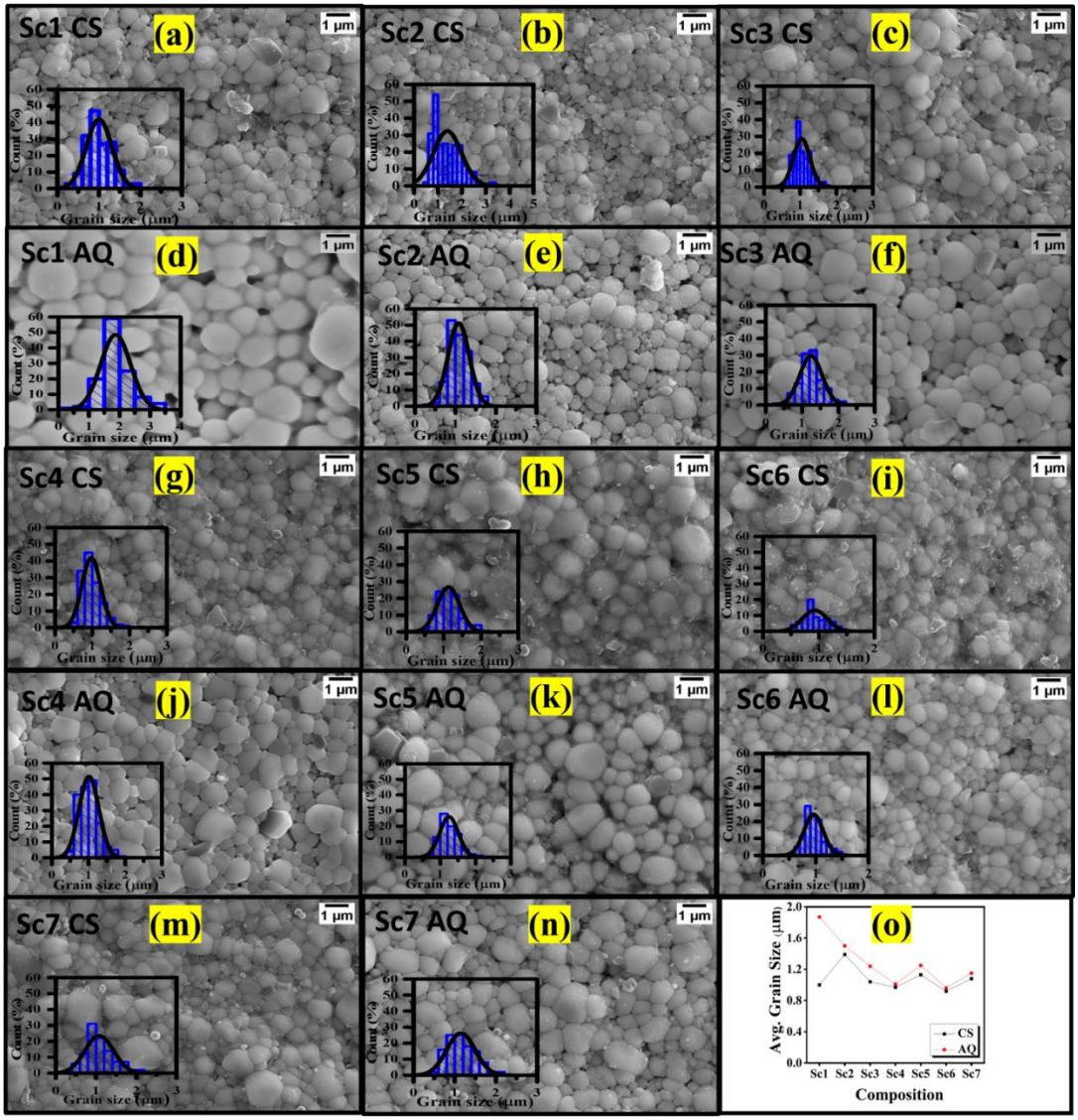

Figure 3.8 SEM micrographs of 0.67{Bi($Fe_{0.97}Ga_{0.03}$)$_{1-x}Sc_xO_3$}-0.33($BaTiO_3$ ceramics, both air quenched (AQ) and closed sintered (CS) samples sintered at 960ºC for 2 hours (a-d) x=0.01, (b-e) x=0.02, (c-f) x=0.03, (g-j) x=0.04, (h-k) x=0.05, (i-l) x=0.06 and (m-n) x=0.07, along with the corresponding grain size distribution is shown in the insets; (o) average grain size variation with respect to the composition for CS and AQ samples.

It suggests that the cooling rate has an important influence on the microstructure of the ceramics, which further affects the crystal structure, ferroelectric, dielectric, and piezoelectric properties [199], [200], [201]. There is a minimal influence of Sc^{3+}

concentration on the microstructure of the ceramics even though average grain size remains almost unaltered even when concentration is increased up to 5 mol % of Sc; this may be due to the rare earth ion Ga substitution, which previously has been reported to suppress the grain growth and act as an inhibitor in grain growth of perovskites because of their low diffusivity [202], [203]. This behavior can be attributed to the isovalent substitution of Sc^{3+} at B site (Fe^{+3}) site which is believed to enhance the chemical stability in perovskites previously [204]. The fine grain microstructure has previously been reported to guarantee high mechanical strength and electromechanical properties without scaling effect, which can be beneficial for high-frequency transducer applications [205], [206], [207].

3.3.3 Electrical Characterizations

3.3.3.1 Dielectric Properties

The temperature-dependent dielectric permittivity and loss (tanδ) were systematically investigated over a wide temperature range of 30 ℃ to 500 ℃, covering a broad frequency range from 20 Hz to 10 MHz, to understand the effects of the processing method and composition on the ferroelectric phase transitions of these ceramics. Figure 3.9 shows the comprehensive dielectric behavior as a function of temperature and processing method at selected frequencies for the prepared compositions. The strong frequency dependence of the real part of permittivity vs. temperature curve is attributed to the relaxor ferroelectric-like behavior consistent with the structural studies that suggest the pseudocubic symmetry for AQ samples and pseudocubic phase as one of the major phases for CS samples. The peaks corresponding to maxima in permittivity vs. temperature curve in CS and AQ samples for the $x \leq 0.03$ was not observed up to 500 ℃ which signifies T_m should be above this value.

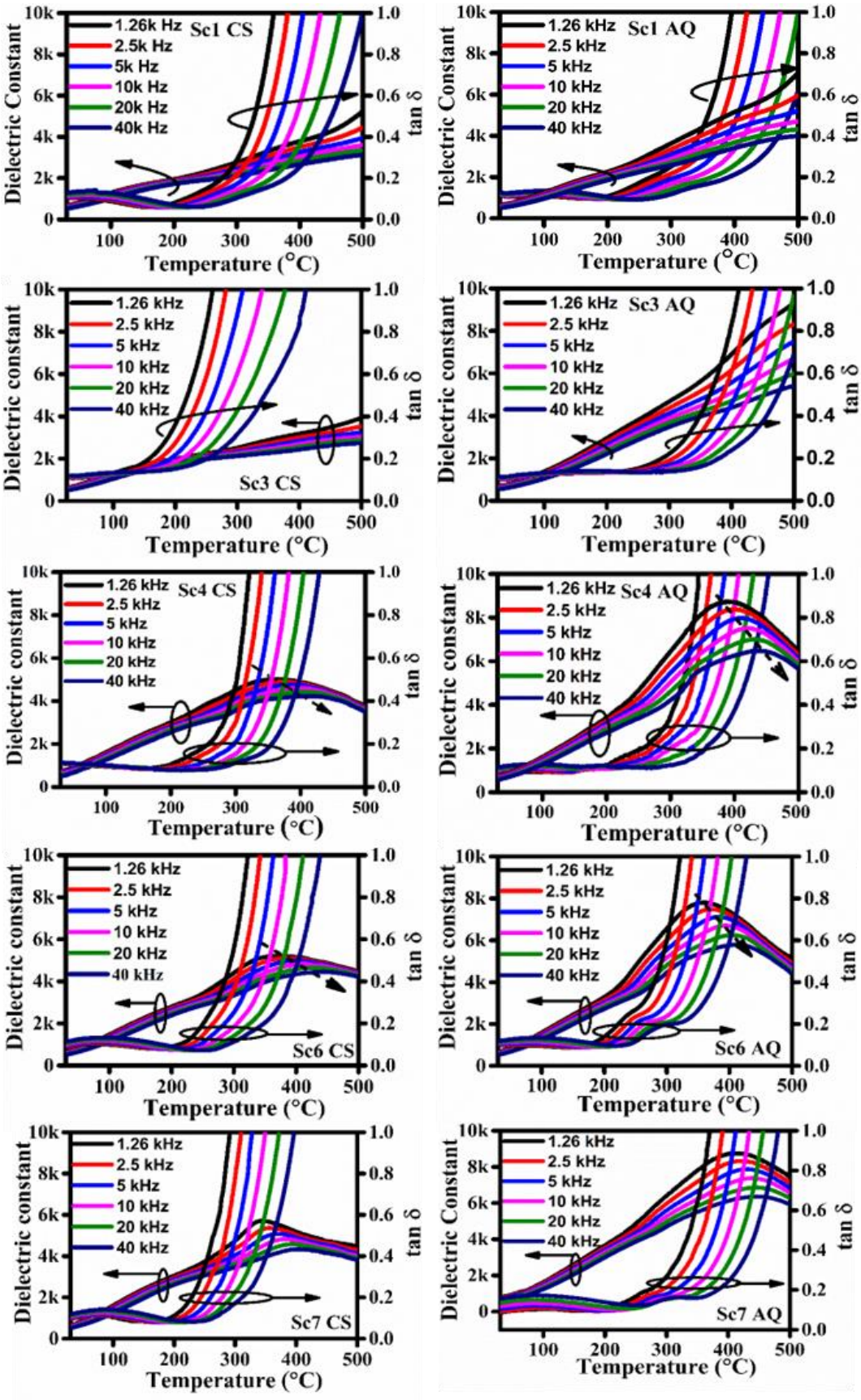

Figure 3.9 Comparison of temperature-dependent dielectric permittivity (ε_r) and loss (tan δ) at

various frequencies for $0.67\{Bi(Fe_{0.97}Ga_{0.03})_{1-x}Sc_xO_3\}$-$0.33(BaTiO_3)$ samples prepared using AQ and CS methods.

For further increased doping concentration of Sc ($0.03 \leq x \leq 0.07$), T_m remains less than 400 ℃ for CS samples when compared at 10 Hz. However, the T_m values of 423 ℃, 396 ℃ and 443℃ were obtained in Sc4 AQ, Sc6 AQ and Sc7 AQ samples respectively. In a similar study Wan et al. reported that for $x < 0.03$, Sc^{+3} substitutes for Fe^{+3} resulting in increased T_c but on further increasing the doping concentration of Sc^{+3}, it substitutes Bi^{+3} leading to creation of B site vacancies (V_{Fe}''') [183]. The latter part may not be applicable to our study since we incorporated 5 mol% excess Bi_2O_3 to compensate for any volatilization effects. Furthermore, at lower temperatures, the increased dissipation factor reveals distinct features attributable to contributions from heterogeneous regions. In systems characterized by a higher volume proportion of the heterogeneous regions, a greater loss maximum is observed as it is associated with the polarization switching [208].

Previous studies on relaxor materials have demonstrated that the presence of a mixed FE-PE (ferroelectric-paraelectric) like unit cell contributes to enhanced flexibility in polarization rotations and enables ultrahigh piezoelectric response over a wide temperature range [209]. The B-site isovalent substitution involving rare-earth dopants has been a viable approach to enhance local structural heterogeneity, leading to the induction of random fields/bonds and alteration of the ordering degree at the B-site cations [208], [210], [211]. Local structure heterogeneity can result in the formation of regions with different local atomic arrangements, known as polar nano regions (PNRs). PNRs are regions within the crystal where the local dipole moments are not perfectly aligned. The presence of PNRs gives rise to relaxor-like behavior.

The broader relaxation times associated with the diverse size distribution of PNRs are responsible for the higher dielectric constant and lower loss factor observed at lower

frequencies [212]. Consistent with the general trend, the substitution in the BF-BT system drives the material towards relaxor characteristics due to the presence of competition for uniform displacements on both sites, resulting in a greater driving force required for the formation of short-range ordered pseudo-symmetric structures [66], [100], [213]. This behaviour can be attributed to factors such as isovalent substitution or grain size reduction [181].

Comparing the two sintering methods, the closed sintered samples exhibit minimal dielectric loss within a narrow temperature range of 30-200 ℃. In contrast, the air quenched samples demonstrate a drastic reduction in the dissipation factor as compared to the furnace cooled closed sintered samples, resulting in an extended temperature range up to nearly 300 ℃. This characteristic holds significant benefits for high-temperature applications. Furthermore, the T_m values for the AQ samples are found to be higher than those of the CS samples at the same composition and frequency. This difference can be attributed to the variations in the sintering methods employed, which subsequently influence other functional properties [32]. Moreover, the increased dielectric permittivity values for respective AQ samples are believed to be an obvious consequence of increased grain size and reduced oxygen vacancies [184]. This can be explained by the fact that air quenching avoids the intermediate temperature range (447 ℃- 767 ℃), which is typically associated with the formation of defects or secondary phases [102]. Although relaxor ferroelectrics may not exhibit an extensive direct piezoelectric charge coefficient (d_{33}), they can possess a significant indirect piezoelectric charge coefficient (d_{33}^*) [214]. This characteristic makes them suitable for applications involving actuation, energy storage, electro-caloric effects, and more.

By elucidating the intricate interplay between composition, processing method, and functional properties, this study provides valuable insights into the design and

optimization of relaxor features of the ferroelectric materials. The possibility of broad stable temperature range at high temperature in contrast to typical ferroelectric behavior contribute to their potential for various advanced applications.

3.3.3.2 Ferroelectric and Piezoelectric properties

Pure BF-BT ceramics typically exhibit unsaturated P-E (polarization-electric field) hysteresis loops due to poor insulation caused by leakage current and high dissipation factor [100], [196]. According to previous reports the substitution of Sc^{+3} for Fe^{+3} at B site enhances ferroelectric properties as it stabilizes the ferroelectric distortion by forming Sc 3d-O 2p hybridization [183]. However, by conducting the measurements at a specific frequency of 10 Hz, nearly well-saturated P-E loops were obtained for all prepared compositions, with even further enhancement observed in the air quenched (AQ) samples, as clearly depicted in Figure 3.10.

The current response loop enables the precise measurement of coercive field, E_c by stipulating switching peaks. Figure 3.11 (a-c) displays the P-E loops along with the corresponding current response loops for AQ samples with Sc- concentrations of 2, 3, and 4 mol %. The presence of two switching peaks in the current response loops indicate the existence of a reversible electric-field-induced ferroelectric (FE) phase. These results strongly indicate the beneficial role of thermal air quenching in improving the polarization switching characteristics and enhancing the ferroelectric properties. To provide a comprehensive overview, Figure 3.11 (d) presents the compiled values of remnant polarization (P_r) and coercive field (E_c) for all the samples. It is evident that the P_r and E_c values of all AQ samples are slightly higher than those of the corresponding CS samples, except for the Sc4 CS sample, which exhibits a lossy nature as clearly observed in Figure 3.10 (a).

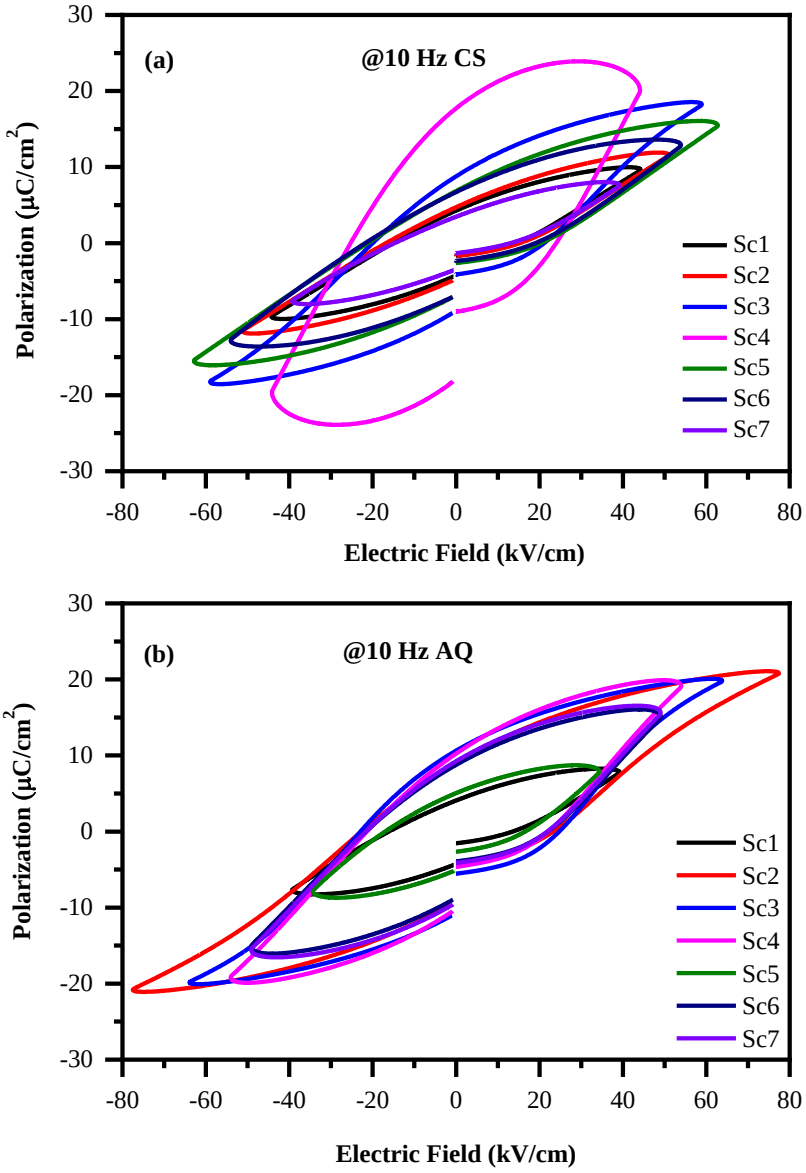

Figure 3.10 Room temperature ferroelectric polarization (P)-electric field (E) hysteresis loops at 10 Hz for (a) closed sintered (CS) samples and (b) air quenched (AQ) samples, as a function of composition.

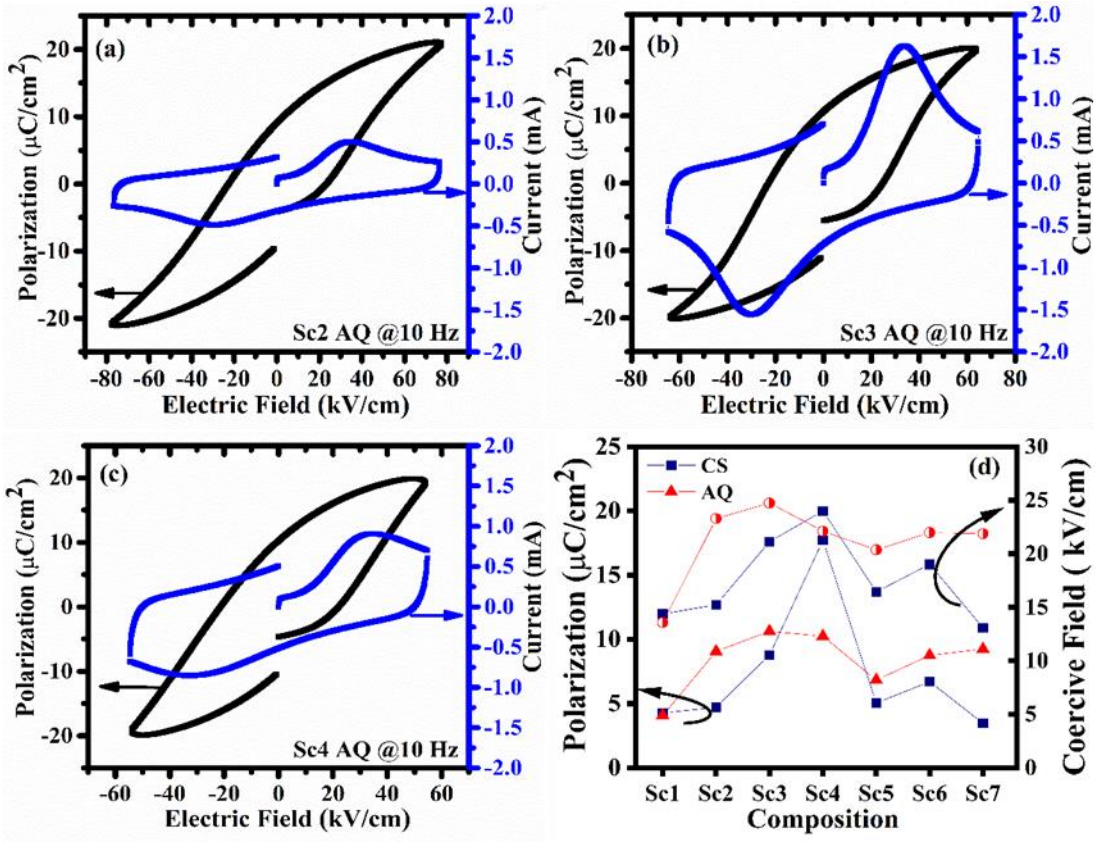

Figure 3.11 Ferroelectric polarization (P-E) hysteresis loop along with corresponding current response at 10 Hz for (a) Sc2 (b) Sc3 (c) Sc4 samples prepared by AQ method, and (d) remnant polarization (P_r) and coercive field (E_c) as a function of composition for CS and AQ samples.

The reduced E_c values can be attributed to smaller grain sizes resulting from rare earth ion substitution, which diminishes the domain width and facilitates easier movement of ferroelectric domains. The P_r/P_s ratio of all AQ samples was greater than that of corresponding CS samples except for Sc4 again due to the lossy hysteresis loop of Sc4 CS, which indicates the nonreversible nature of the ferroelectric domain on the removal of an applied electric field [188]. The behavior of Sc4 CS sample is somewhat inconsistent for the P-E response due to some unknown reasons.

A comparison of current response curves for AQ and CS, as shown in Figure 3.12, reveals well-defined switching behavior, evidenced by peaks near 30 kV/cm. This confirms the saturation of the P-E loops and lower coercive fields for AQ samples. Such behavior was

absent in the conventionally sintered samples, indicating an inferior ferroelectric (FE) phase. These observations align with previous reports by Kim et al., highlighting the enhanced ferroelectric domain switching behavior achieved through the thermal air quenching process [199].

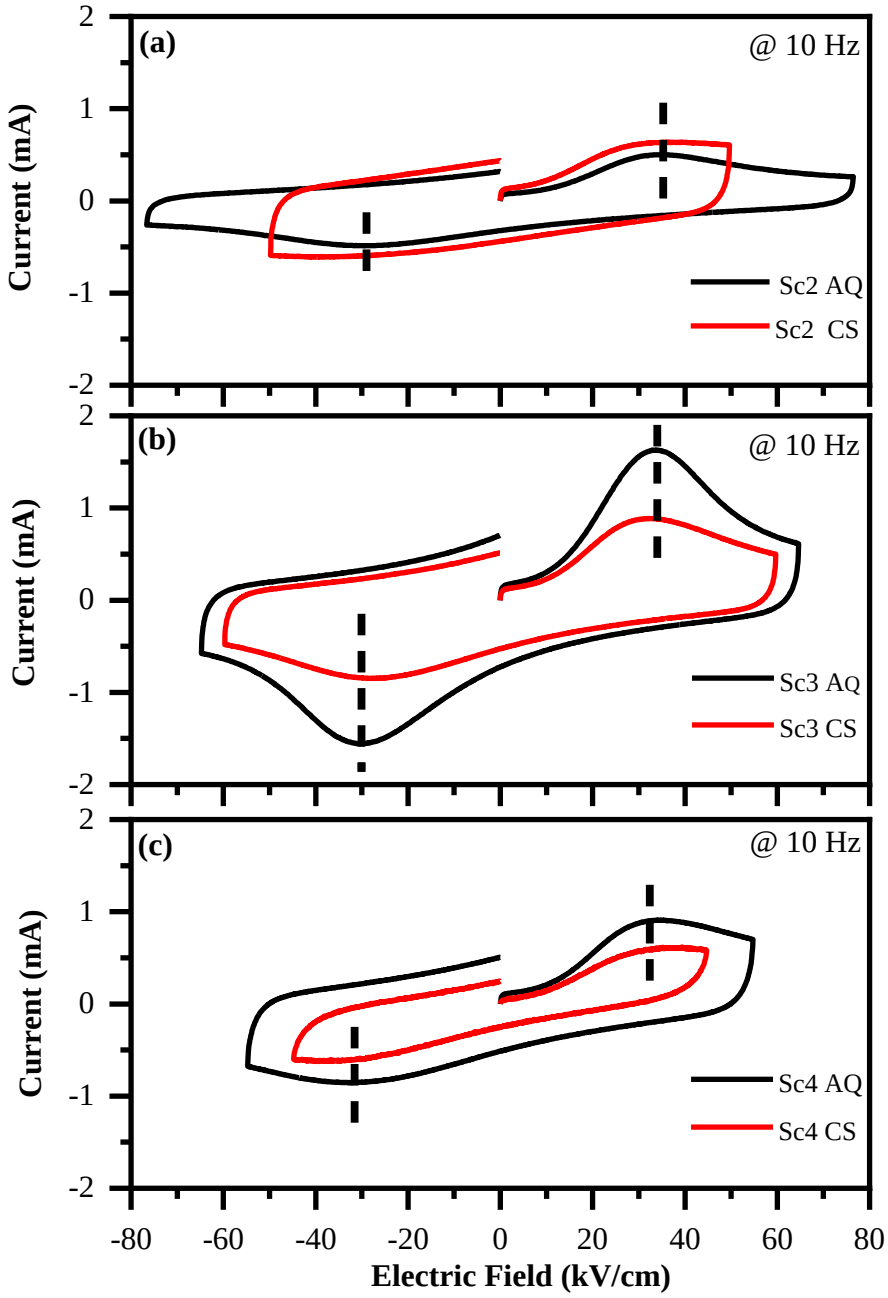

Figure 3.12 Current response curves for (a) Sc2 CS and Sc2 AQ, (b) Sc3 CS and Sc3 AQ, (c) Sc4 CS and Sc4 AQ.

However, the exact underlying mechanism behind this phenomenon remains incompletely understood and warrants further investigation using advanced thermodynamic and kinetic theories coupled with relevant observable processing methods. The leakage current results, depicted in Figure 3.13 (a-b), reveal current and resistivity data for all CS AQ samples Resistivity (measured in ohm·cm) obtained from the leakage current measurements remained consistent across a broad range of applied fields (1-60 kV/cm), exhibiting values on the order of 10^9. It is evident that the increased leakage current density observed in the CS samples is attributed to the presence of oxygen vacancies or Fe reduction, or both, which adversely affect the ferroelectric and piezoelectric properties [215]. In contrast, the AQ samples exhibit a higher oxygen partial pressure compared to the sintering atmosphere in CS because of closed sintering atmosphere, leading to reduced vacancy defects and consequently improved properties.

The impact of processing methods on the piezoelectric charge coefficient (d_{33}) is evident in Figure 3.13 (c). This figure unequivocally demonstrates that the d_{33} values obtained for AQ samples are notably higher as compared to CS samples for all the compositions. The Sc3 AQ sample, with a density of 7.35 g/cm3 and poled at 40 kV/cm at 80 ℃ for 30 minutes, achieved the maximum d_{33} value of 35 pC/N.

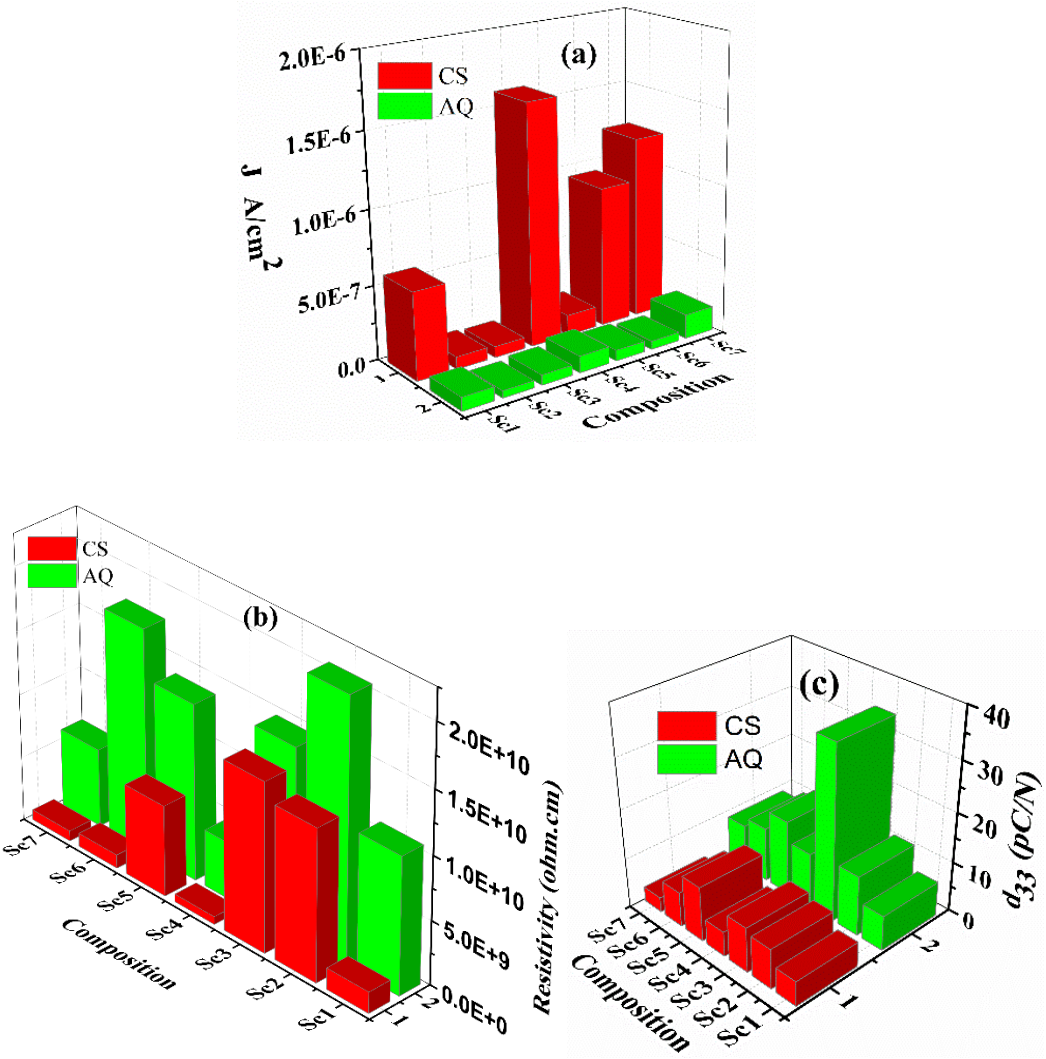

Figure 3.13 (a) Current density J (A/cm^2) and (b) Resistivity (ohm.cm) plots with respect to composition for both AQ and CS specimens at 1 kV/cm of applied electric field and (c) comparison of piezoelectric charge coefficient, d_{33} for AQ and CS samples for different compositions.

4. Conclusion

In conclusion, we successfully synthesized novel lead-free Sc, Ga-modified BF-BT polycrystalline piezoceramics and systematically investigated the impact of closed sintering and air quenching methods on their structural, functional, and electrical properties. The ceramics prepared using the air quenching method exhibited significant improvements in resistivity (of the order of 10^{10}), P_r (ranging from 4-11 µC/cm^2), P_s (ranging from 8-21 µC/cm^2), T_m (greater than 400 ºC), E_c (ranging from 13-25 kV/cm), reduced dielectric loss, and enhanced dielectric permittivity across a wide temperature

range as compared to closed sintered samples. These findings highlight the substantial influence of the processing method on the properties of the BF-BT based piezoelectric systems. The observed small grain size, favorable ferroelectric properties, and relaxor-like behavior suggest the potential for achieving significant piezoelectric strain properties in the developed material. Moreover, the broad frequency-dependent dielectric behavior and reduced values of P_r and E_c further support the relaxor-like characteristics. The decreased P_r values make these materials suitable for energy storage applications, while the reduced hysteresis benefits actuation purposes. Overall, this study emphasizes the importance of understanding ceramic processing methods for the development of high-performance lead-free BF-BT based piezoceramics.